

## Supplemental Information

### The geography of climate change: implications for conservation biogeography

D.D. Ackerly, S.R. Loarie, W.K. Cornwell, S.B. Weiss, H. Hamilton, R. Branciforte and N.J.B. Kraft

*Diversity and Distributions*, 2010

#### Climate and climate change data:

Present climate surfaces in this study were derived from PRISM 30 arc-second historical norms (1971-2000) (Fig. S1). Monthly mean temperatures were calculated as the mean of minimum and maximum temperatures, and then averaged to provide mean annual temperature. Temperatures seasonality was calculated as the standard deviation of monthly mean values for each pixel. Monthly precipitation was summed to obtain total annual precipitation, and seasonality was calculated as the coefficient of variation of monthly rainfall (CV was chosen to adjust for shifts in the mean from dry to wet regions).

For area histograms, the average pixel size was set at 0.67 km<sup>2</sup>, the average size of 30 arc second pixels calculated at the southern (33°N) and northern (44°N) edges of our domain, based on the formula:

$$A = (111.325 * C) * (\cos(\text{lat} * \pi / 180) * 111.325 * C)$$

where A is pixel size (km<sup>2</sup>), C is pixel size in fractions of a degree, and lat is latitude. The first term is the latitudinal dimension of the pixel (111.325 km/degree) and the second term is the longitudinal dimension, which shrinks from a maximum at the equator to zero at the poles. Note that the 800 m PRISM surface is often referred to as 1 km resolution, for convenience, but actual pixel size is considerably less than 1 km<sup>2</sup>, especially as one moves towards the poles.

#### *Uncertainty and comparability of climate surfaces*

Given the increasing importance of climate surfaces in hydrological and ecological analyses, relatively little emphasis has been placed on their evaluation. All current climate surfaces are generated by algorithms which produce gridded data from a smaller set of observations, usually weather station records (Daly, 2006; Daly *et al.*, 2008). These point observations are sparse, especially in sparsely populated areas, and biased toward low elevations. In regions of low weather station density and/or high topographic complexity, the uncertainty introduced by such extensive interpolation may be significant.

A variety of current climate surfaces are available, offering a range of observed and derived climate variables with varying methods of interpolation, levels of spatial resolution, geographic coverage, and uncertainty. The most widely used are PRISM and Daymet (Thornton *et al.*, 1997) for the continental United States and Canada, and WorldClim (Hijmans *et al.*, 2005) and the East Anglia CRU climate data (<http://www.cru.uea.ac.uk/>) for global analysis. Few comparisons exist of the values for environmental parameters produced by alternative climate surfaces (Daly, 2006; Daly *et al.*, 2008; Loarie *et al.*, 2009). No studies have yet systematically examined the implications of using alternative current climate surfaces as modeling inputs.

Many ecological studies generate future climate surfaces for impact analyses using simple downscaling methods that calculate change factors between current and future modeled climate parameters and interpolate these to a current climate surface at the desired spatial resolution. There is additional, though difficult to quantify, uncertainty introduced at this step (Klausmeyer and Shaw, 2009; Lawler, 2009). High resolution future climate surfaces generated directly from climate model outputs are available only for limited geographies (Maurer *et al.*, 2007), such as those employed in analyses presented here for the conterminous U.S. These current and future climate surfaces are essential tools for forecasting climate impacts across geographies and in a wide variety of sectors (e.g., Diffenbaugh *et al.*, 2008; Loarie *et al.*, 2008; Lawler, 2009; Loarie *et al.*, 2009; Parisien and Moritz, 2009). Yet, the level of uncertainty in downscaled climate surfaces is unknown. In part because of heterogeneity of modelling approaches, no systematic effort has explored these uncertainties, or how they are propagated through to outcomes of modeling efforts.

The geography of climate change will be much better understood when a standardized set of global high resolution current and future climate surfaces are available for a wide range of climate modeling studies. In the interim, a detailed comparative analysis of the wide range of existing current climate surfaces would provide a better understanding of the differences among these climate datasets and how that might affect the many modeling efforts which they underlie. The work presented in this paper is no less subject to these issues, as we utilize the PRISM gridded, spatial data set; we recognize that analyses such as ours will require continued analysis using alternative data sources to determine the robustness of conclusions.

#### *Future climate projections*

We acquired bias-corrected and spatially downscaled future climate projections from the World Climate Research Programme's (WCRP's) Coupled Model Intercomparison Project phase 3 (CMIP3) multi-model dataset through the LLNL-Reclamation-SCU downscaled climate projections derived from the WCRP's CMIP3 multimodel dataset, stored and served at the LLNL Green Data Oasis (Wood *et al.*, 2002; Wood *et al.*, 2004; Maurer, 2007). From these, we calculated mean annual temperature and total annual precipitation from the A1B emission scenario averaged over the time period from 2070-2099. These data are downscaled to 1/8<sup>th</sup> degree spatial resolution. Average change in temperature and temperature seasonality over 16 general circulation models in the CMIP3 dataset are shown in Fig. S2. Projected change in precipitation, which varies considerably over our domain, is shown for each of the models in Fig. S3. We selected the CCCMA\_CGCM3\_1.1 and GFDL\_CM2\_1.1 models, representing warmer-wetter and warmer-drier scenarios, respectively (Fig. S3, highlighted; maps for mean annual temperature and total annual precipitation shown in Fig. S4).

#### *Historical variability*

Historical climate surfaces for 1971-2000 obtained from PRISM were analyzed to determine the standard deviation of interannual variation for mean annual temperature and total precipitation, in each pixel (Fig. S5). Variability in temperature was lowest along the California coast, and higher in the interior, Several small hotspots scattered across the map suggest possible interpolation errors across years, or changes in data

availability. Variability in precipitation was lowest in the Great Basin, and highest in the small corner of the Mojave desert in our domain. Average values of variability were calculated across the entire domain, and used to establish the width of histogram bins for calculation of changes in the realized climate (see text, Fig. S6). Maps of temperature and precipitation with color schemes following these histogram bin widths are shown in Fig. S7.

#### *Velocity magnitude and direction calculations*

To estimate climate change velocity ( $\text{km yr}^{-1}$ ), we calculated the ratio of spatial ( $^{\circ}\text{C km}^{-1}$  and  $\text{mm km}^{-1}$ , for temperature and precipitation respectively) and temporal gradients ( $^{\circ}\text{C yr}^{-1}$ ;  $\text{mm yr}^{-1}$ ) (Loarie *et al.*, 2009). We calculated the magnitude of spatial gradients on the present climate surfaces with a 3-by-3 grid cell neighbourhood using the average maximum technique (Burrough and McDonnell, 1998, p. 190) modified to accommodate different cell-widths at different latitudes. To convert cell-height in latitudinal degrees to km, we used  $111.325 \text{ km degree}^{-1}$ . To convert cell-width in longitudinal degrees to km we calculated  $\cos\left(\frac{\pi}{180}y\right) 111.325$  where  $y$  is the latitude of the pixel in degrees. We used an analogous aspect algorithm to estimate the axis of the spatial gradients for each 3-by-3 grid cell (Burrough and McDonnell, 1998).

We approximated temporal gradients by resampling the  $1/8^{\text{th}}$  degree future climate surfaces to the PRISM 30 arc-second grid and subtracting the present climate surfaces from the future surfaces divided by 100. We used these temporal gradients to calculate velocity magnitudes by taking the ratio of the spatial and temporal gradients (Fig. S8a-c). To estimate the direction of climate change, we defined a unit vector along the directional axis of the spatial gradient pointed opposite sign of the temporal gradient. For example, if temperature increases, we picked the direction pointing towards cooler climates (Fig. S8d-f).

For rising temperatures, compensatory movement should occur towards decreasing values on the current landscape (e.g., upslope). Given the topographic complexity of California, the predicted directions of movement in response to temperature are complex and highly interdigitated (Fig. S8d). The general northeasterly trend along the west slope of the Sierra Nevada is evident. For precipitation, the direction of movement depends critically on whether climate change will lead to drier or wetter conditions, as the direction at any point on the landscape will reverse  $180^{\circ}$  if the direction of climate trends reverses. This reversal is evident in the mirror image of colors for precipitation for the warmer-drier vs. warmer-wetter scenarios (Fig. S8 e vs. f). Under the warmer-wetter scenario, compensatory movements in response to temperature and precipitation change are generally conflicting, as seen by contrasting color patterns (Fig. S8d vs f) across a regional reserve network.

#### **Climate variability of reserves**

Protected areas of the Bay Area Protected Area Database (BPAD) were combined using the ARCMAP dissolve function, with a 100 m threshold, to identify contiguous reserves. All areas larger than 125 ha (2 PRISM pixels) were maintained for analysis, resulting in a set of 538 reserves. Reserve polygons were rasterized and aligned with PRISM climate surfaces for analysis.

Climate diversity was calculated using Rao's quadratic entropy. Rao's entropy is usually calculated using the distribution of relative abundances ( $p_i$ ) in  $N$  discrete classes with dissimilarities among classes in distance matrix  $d_{ij}$ :

$$S = \sum_{i=1}^{N-1} \sum_{j=i+1}^N d_{i,j} p_i p_j$$

Alternatively, for the climate surfaces considered here, each of the  $N$  pixels can be treated as its own class, so  $p_i = 1/N$ , and the formula reduces to:

$$S = \frac{\sum_{i=1}^{N-1} \sum_{j=i+1}^N d_{i,j}}{N^2}$$

### Acknowledgements:

We acknowledge the climate modeling groups, the Program for Climate Model Diagnosis and Intercomparison (PCMDI) and the WCRP's Working Group on Coupled Modelling (WGCM) for their roles in making available the WCRP CMIP3 multi-model dataset. Support of this dataset is provided by the Office of Science, U.S. Department of Energy.

### Literature Cited

- Burrough, P.A. & McDonnell, R.A. (1998). *Principles of geographic information systems*. Oxford Univ. Press, Oxford.
- Daly, C. (2006) Guidelines for assessing the suitability of spatial climate data sets. *International journal of climatology*, **26**, 707-721.
- Daly, C., Halbleib, M., Smith, J.I., Gibson, W.P., Doggett, M.K., Taylor, G.H., Curtis, J. & Pasteris, P.P. (2008) Physiographically sensitive mapping of climatological temperature and precipitation across the conterminous United States. *International journal of climatology*, **28**, 2031-2064.
- Diffenbaugh, N.S., Giorgi, F. & Pal, J.S. (2008) Climate change hotspots in the United States. *Geophysical Research Letters*, **35**, L16709.
- Hijmans, R.J., Cameron, S.E., Parra, J.L., Jones, P.G. & Jarvis, A. (2005) Very high resolution interpolated climate surfaces for global land areas. *International journal of climatology*, **25**, 1965-1978.
- Klausmeyer, K.R. & Shaw, M.R. (2009) Climate change, habitat loss, protected area and the climate adaptation potential of species in Mediterranean ecosystems worldwide. *PLoS ONE*, **4**, e6392.
- Lawler, J.J. (2009) Climate Change Adaptation Strategies for Resource Management and Conservation Planning. *YEAR IN ECOLOGY AND CONSERVATION BIOLOGY 2009*, **1162**, 79-98.
- Loarie, S.R., Carter, B.E., Hayhoe, K., McMahon, S., Moe, R., Knight, C.A. & Ackerly, D.D. (2008) Climate change and the future of California's endemic flora. *PLoS ONE*, **3**, e2502.
- Loarie, S.R., Duffy, P.B., Hamilton, H., Asner, G.P., Field, C.B. & Ackerly, D.D. (2009) The velocity of climate change. *Nature*, **00**, 00-00.
- Maurer, E.P. (2007) Uncertainty in hydrologic impacts of climate change in the Sierra Nevada, California, under two emissions scenarios. *Climatic Change*, **82**, 309-325.

- Maurer, E.P., Stewart, I.T., Bonfils, C., Duffy, P.B. & Cayan, D. (2007) Detection, attribution, and sensitivity of trends toward earlier streamflow in the Sierra Nevada. *Journal of Geophysical Research*, **112**,
- Parisien, M.A. & Moritz, M.A. (2009) Environmental controls on the distribution of wildfire at multiple spatial scales. *Ecological Monographs*, **79**, 127-154.
- Thornton, P.E., Running, S.W. & White, M.A. (1997) Generating surfaces of daily meteorology variables over large regions of complex terrain. *Journal of Hydrology*, **190**, 214-251.
- Wood, A.W., Leung, L.R., Sridhar, V. & Lettenmaier, D.P. (2004) Hydrologic implications of dynamical and statistical approaches to downscaling climate model outputs. *Climatic Change*, **62**, 189-216.
- Wood, A.W., Maurer, E.P., Kumar, A. & Lettenmaier, D.P. (2002) Long-range experimental hydrologic forecasting for the eastern United States. *JOURNAL OF GEOPHYSICAL RESEARCH-ATMOSPHERES*, **107**,

### Figure Legends

Fig. S1. (A) Mean annual temperature and (B) annual temperature seasonality (standard deviation of monthly means), both derived from monthly means averaged over historical period (1971-2000). (C) Total annual precipitation ( $\log_{10}$ ) and (D) annual precipitation seasonality (coefficient of variation of monthly means), both derived from monthly means averaged over historical period (1971-2000). Data are from the PRISM interpolated climate database.

Fig. S2. Change in (A) mean annual temperature and (B) temperature seasonality, averaged over 16 GCMs, A1b scenario, for 2070-2099. See Fig. S1a, b for baseline values.

Fig. S3. Projected change in total annual precipitation for 16 GCMs, SRES A1b. Mean values averaged over the domain range from -140 to 272 mm. Ranking them in order we chose the 4<sup>th</sup> and 14<sup>th</sup> models to represent drier and wetter scenarios. Drier: gfdl\_cm2\_1.1, -119 mm; Wetter: cccma\_cgcm3\_1.1, +81 mm. We also used the corresponding temperature projections for these models

Fig. S4. Change in mean annual temperature for (A) GFDL and (B) CCCMA, A1b scenario, for 2070-2099. Change in total annual precipitation for (C) GFDL (warmer-drier) and (D) CCCMA (warmer-wetter), A1b scenario, for 2070-2099. Temperature scale bars are same for Fig. S2A, and Fig. S4A, B.

Fig. S5. Historical variability, measured as standard deviation of annual means from 1971-2000 for (A) mean annual temperature and (B) annual precipitation ( $\log_{10}$  transformed). Mean (range) are 0.58 (0.38 – 1.03) for temperature and 0.15 (0.088 – 0.326) for precipitation.

Fig. S6. Two-dimensional histograms of climate space. A) current; B) warmer-drier scenario (GFDL\_CM2, 2070-2099); C) warmer-wetter scenario (CCCMA\_CGCM3,

2070-2099). See text for procedure used to select bin sizes for each axis. Color intensity corresponds to area occupied by each climate combination. Due to the highly skewed distribution of areas occupied (from 1 to 24000 km<sup>2</sup> for current climate), areas were log-transformed before applying the color scheme.

Fig. S7. Maps of mean annual temperature and total annual precipitation (log<sub>10</sub> transformed) for the 1971-2000 historical period (PRISM). Color breaks correspond to histogram bins in Fig. S6, illustrating geographic distribution of climates that are classified in the same bin for each variable.

Fig. S8. Velocity (left) and direction (right) of climate change for temperature (A, D) and precipitation under the warmer-drier (B, E) and warmer-wetter (C, F) scenarios. Directions represent the direction of movement in space to offset projected changes in climate, and are shown using the compass wheel.

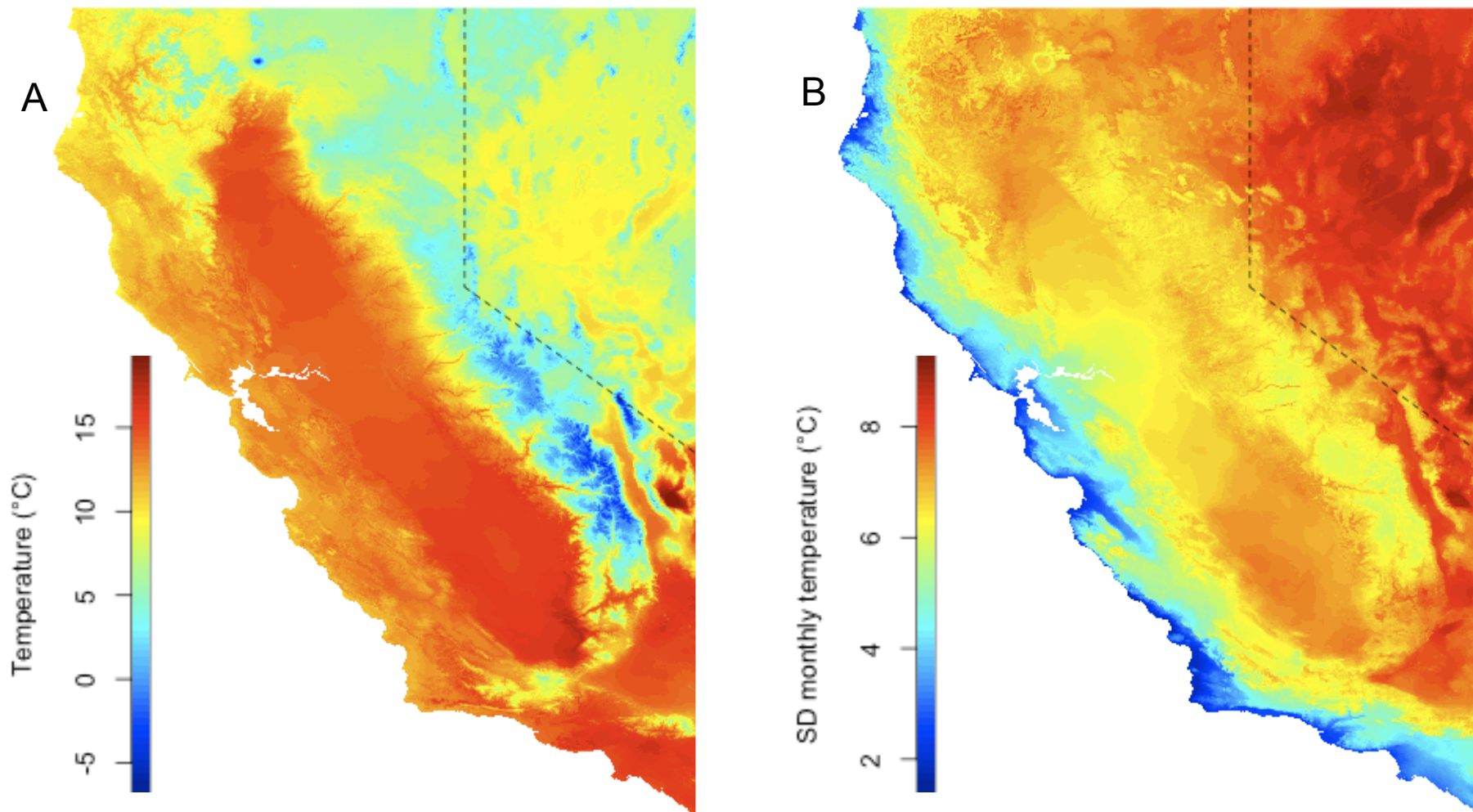


Fig. S1. (A) Mean annual temperature and (B) annual temperature seasonality (standard deviation of monthly means), both derived from monthly means averaged over historical period (1971-2000).

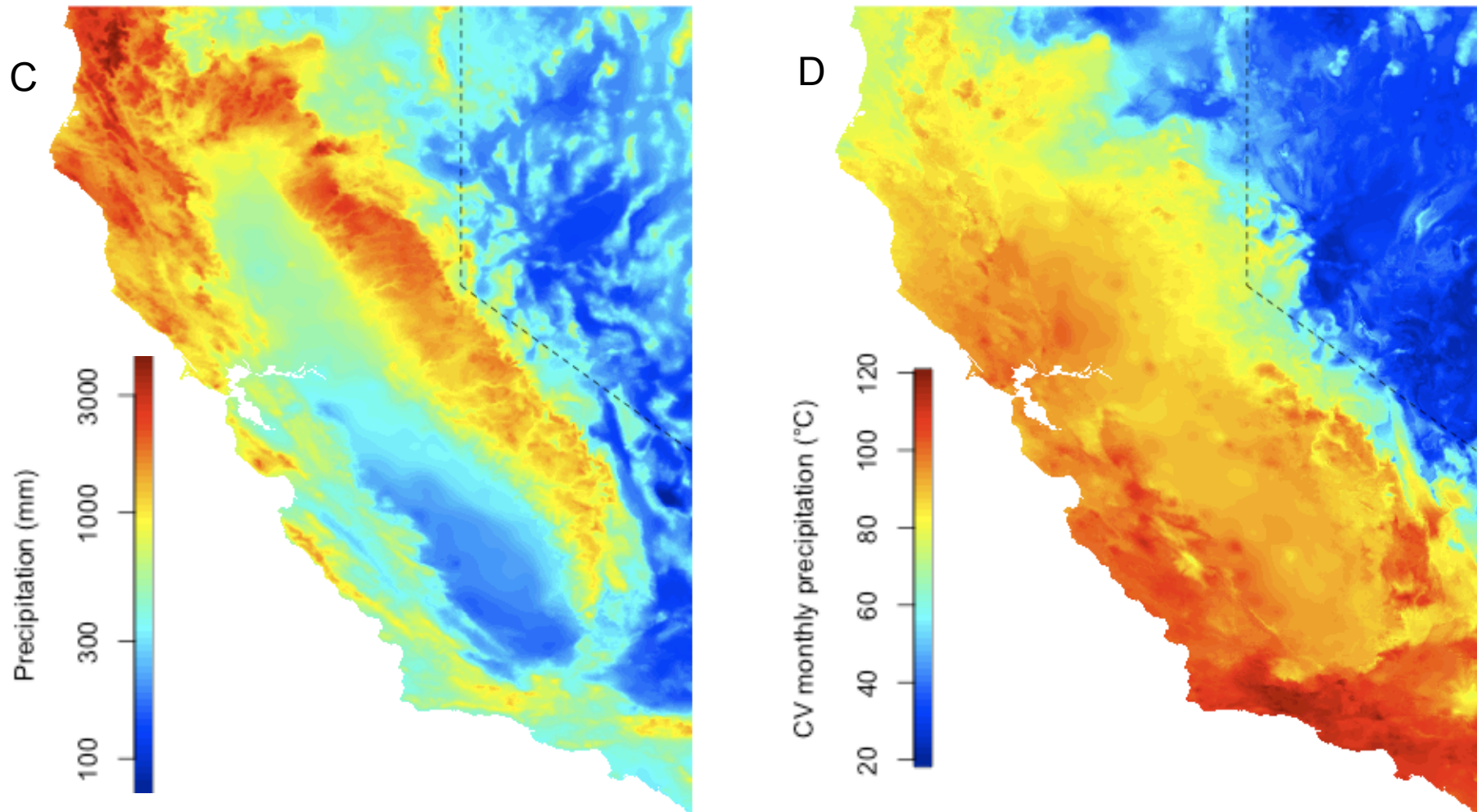


Fig. S1. (C) Total annual precipitation ( $\log_{10}$ ) and (D) annual precipitation seasonality (coefficient of variation of monthly means), both derived from monthly means averaged over historical period (1971-2000). Data are from the PRISM interpolated climate database.

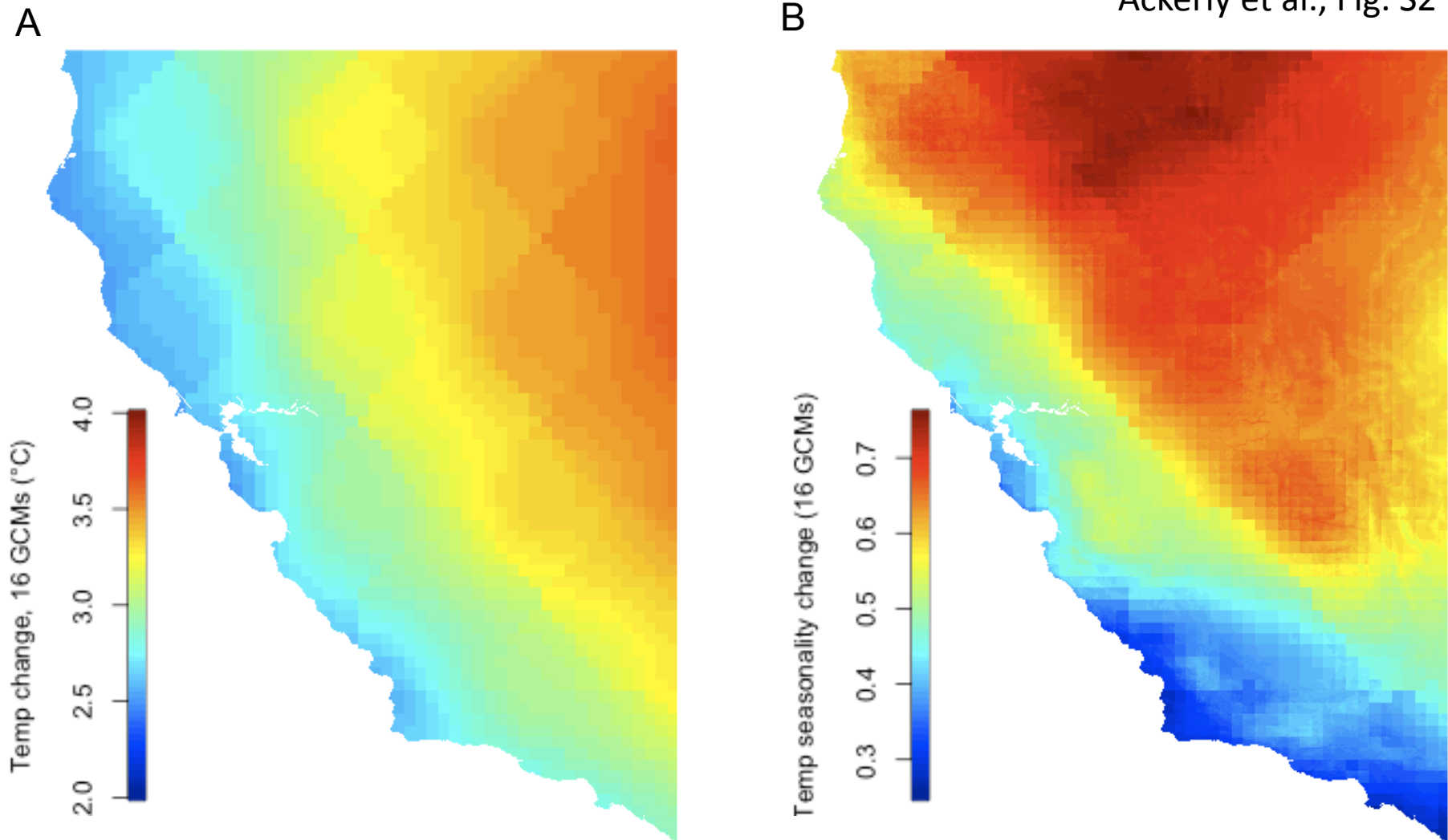


Fig. S2. Change in (A) mean annual temperature and (B) temperature seasonality, averaged over 16 GCMs, A1b scenario, for 2070-2099. See Fig. S1a, b for baseline values.

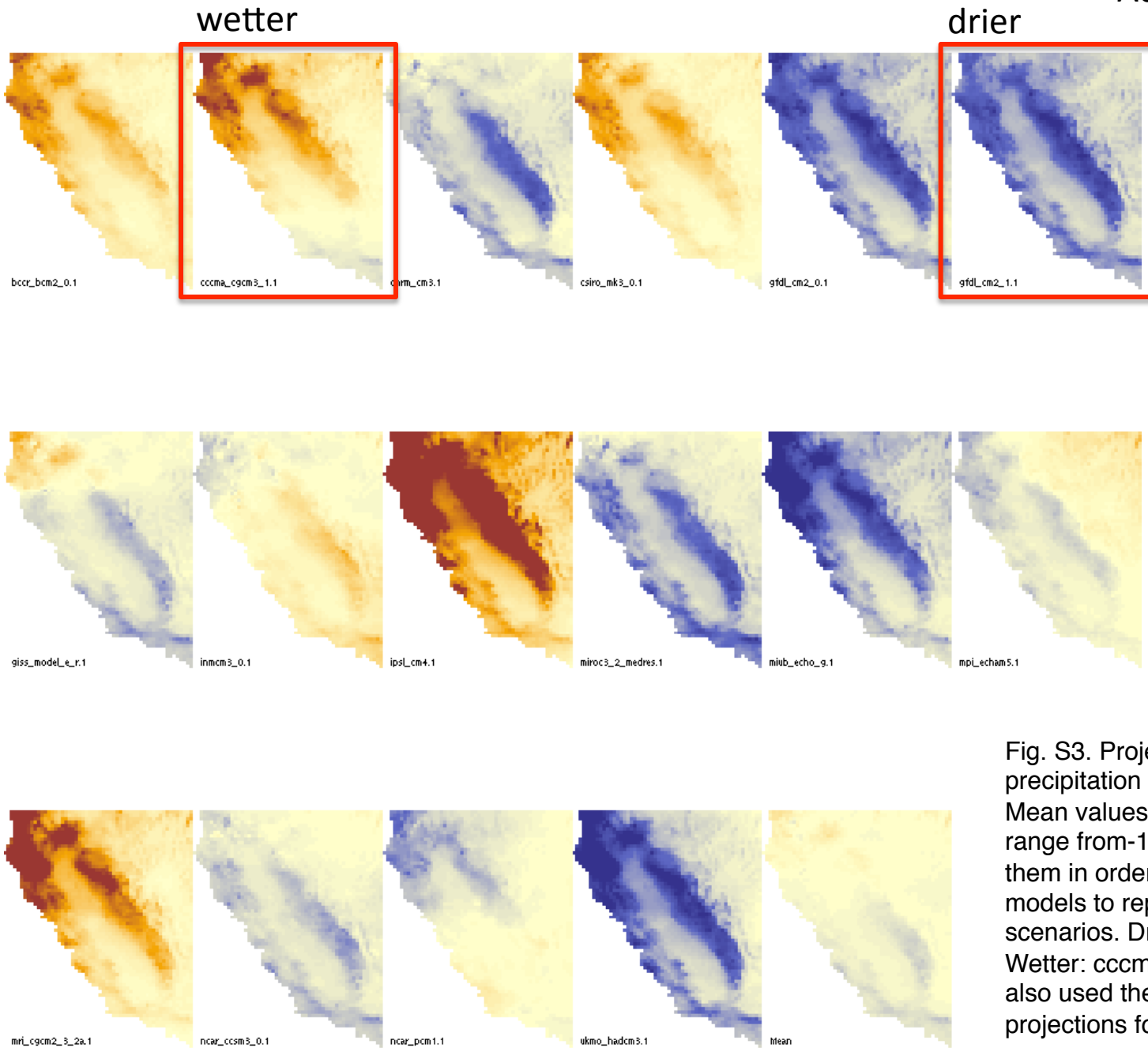


Fig. S3. Projected change in total annual precipitation for 16 GCMs, SRES A1b. Mean values averaged over the domain range from -140 to 272 mm. Ranking them in order we chose the 4<sup>th</sup> and 14<sup>th</sup> models to represent drier and wetter scenarios. Drier: gfdl\_cm2\_1.1, -119 mm; Wetter: cccma\_cgcm3\_1.1, +81 mm. We also used the corresponding temperature projections for these models

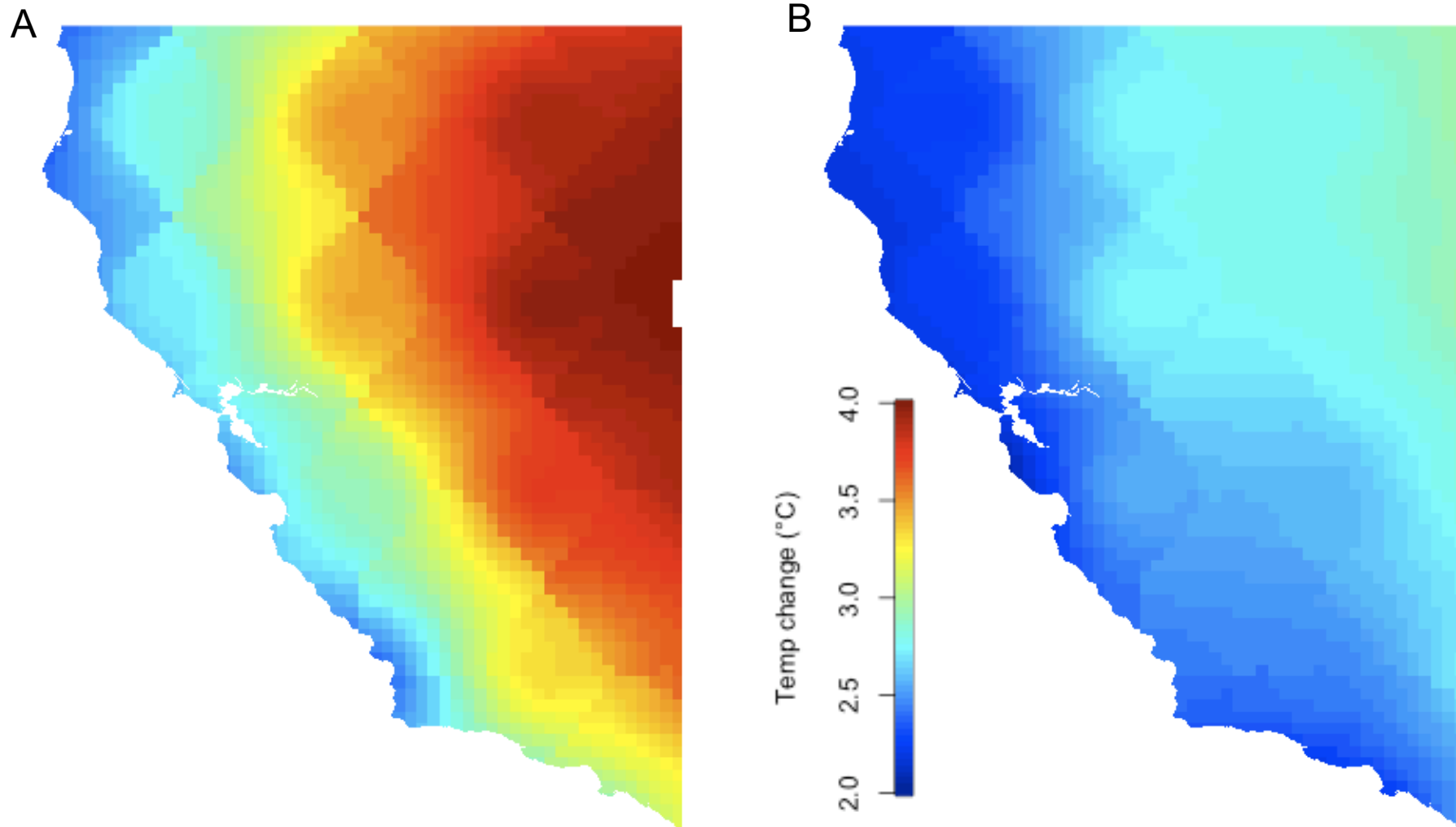


Fig. S4. Change in mean annual temperature for (A) GFDL and (B) CCCMA, A1b scenario, for 2070-2099. Temperature scale bars are same for Fig. S2A, and Fig. S4A, B.

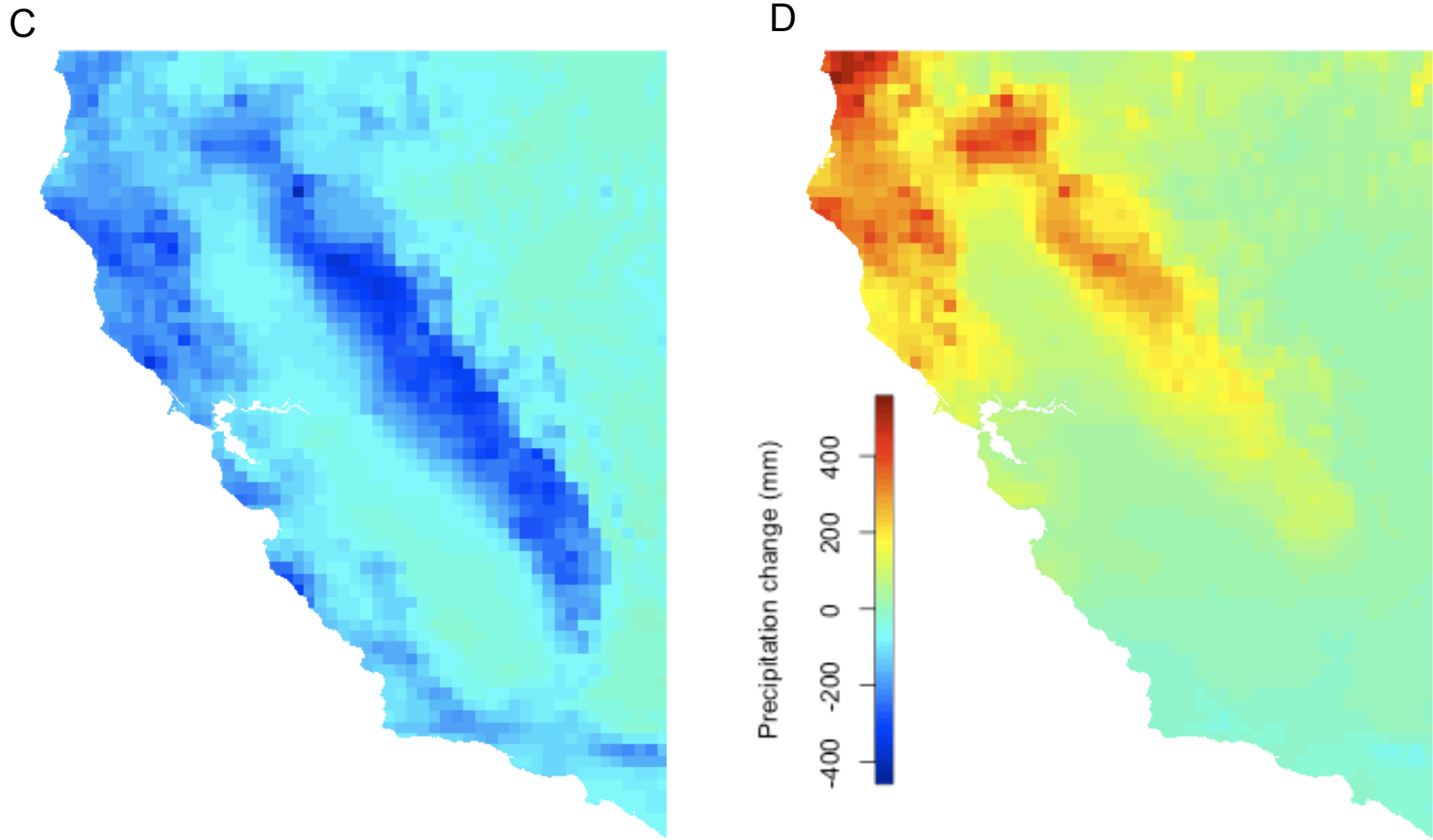


Fig. S4. Change in total annual precipitation for (C) GFDL (warmer-drier) and (D) CCCMA (warmer-wetter), A1b scenario, for 2070-2099.

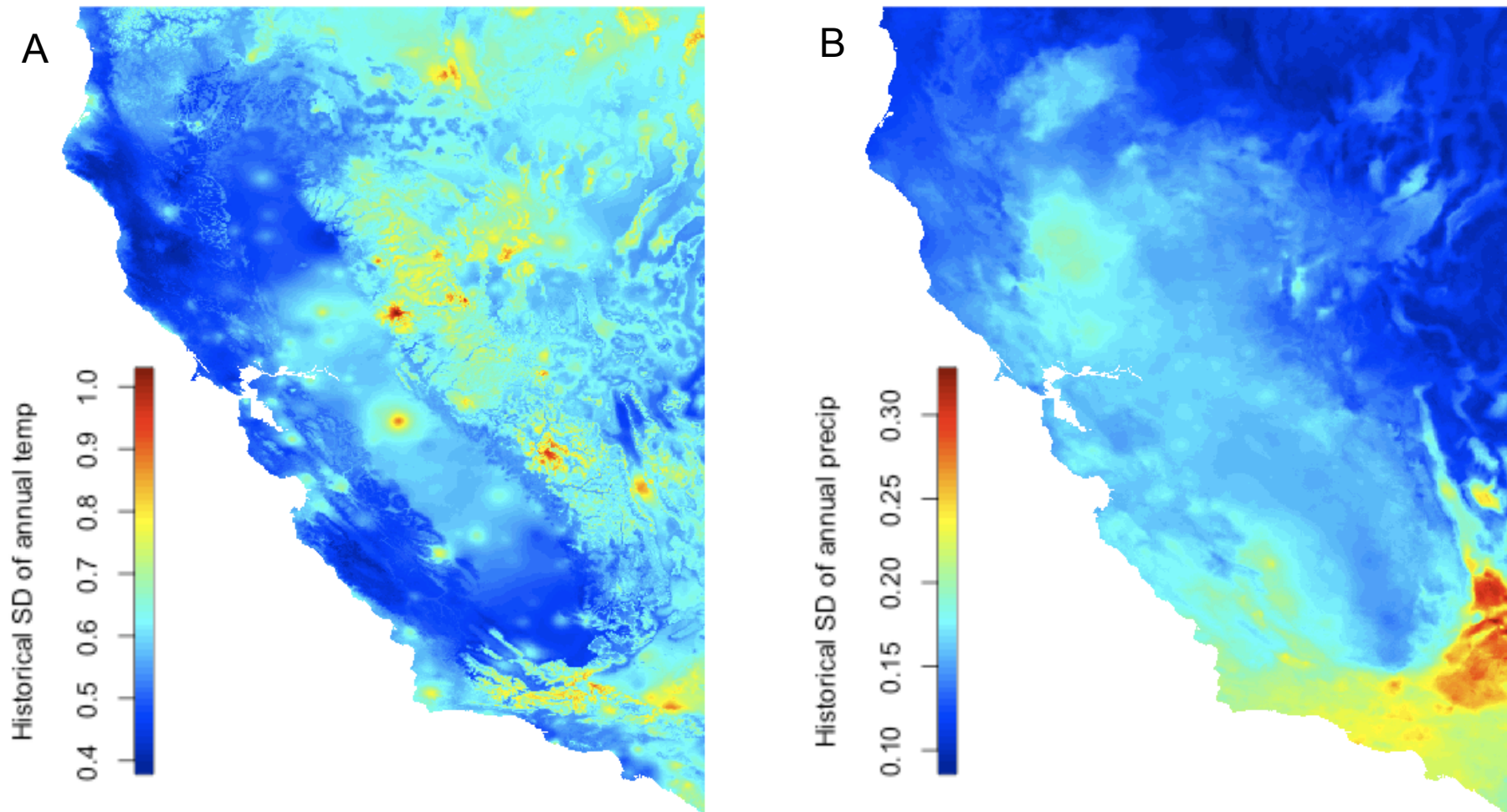


Fig. S5. Historical variability, measured as standard deviation of annual means from 1971-2000 for (A) mean annual temperature and (B) annual precipitation (log10 transformed). Mean (range) are 0.58 (0.38 – 1.03) for temperature and 0.15 (0.088 – 0.326) for precipitation.

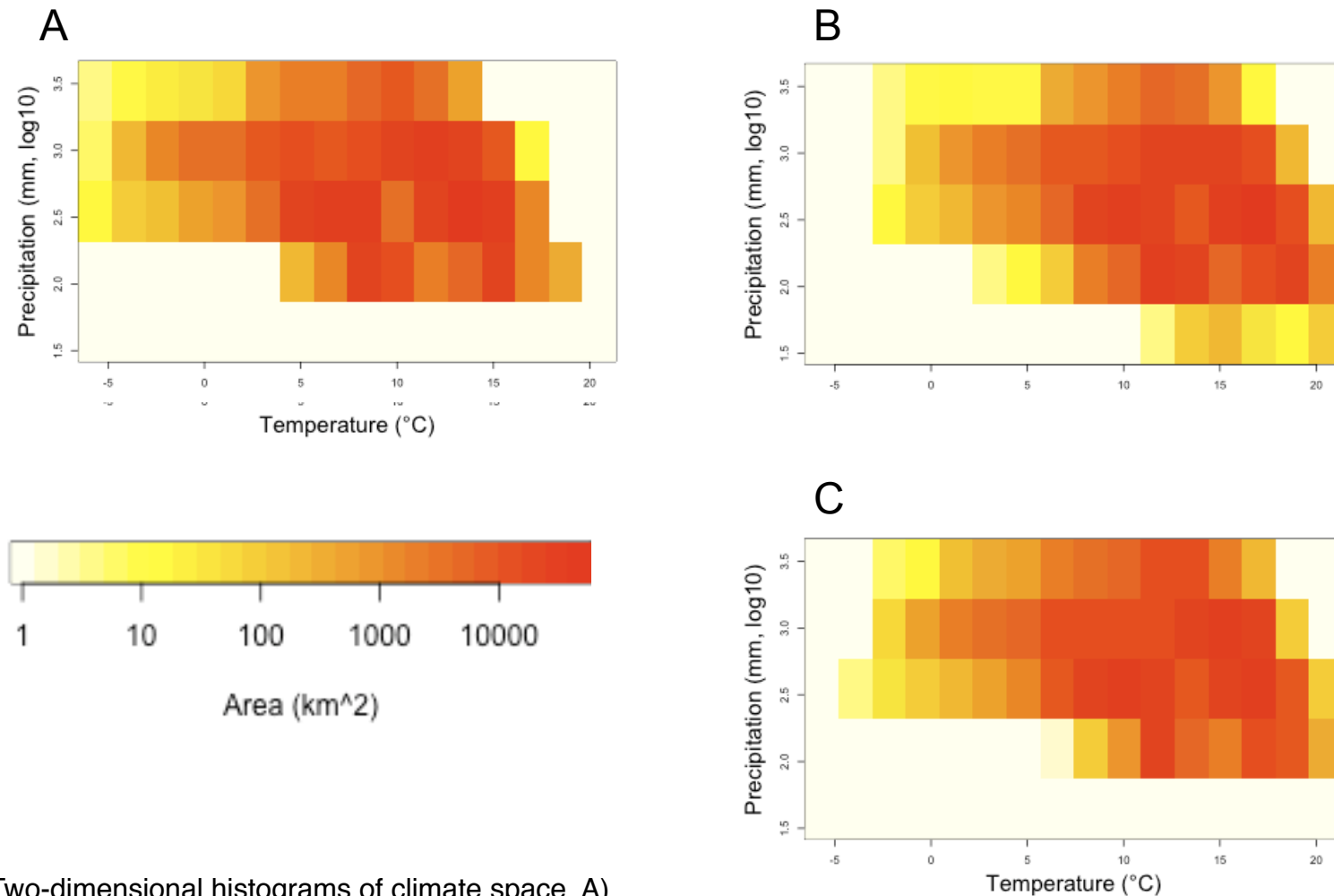


Fig. S6. Two-dimensional histograms of climate space. A) current; B) warmer-drier scenario (GFDL\_CM2, 2070-2099); C) warmer-wetter scenario (CCCMA\_CGCM3, 2070-2099). See text for procedure used to select bin sizes for each axis. Color intensity corresponds to area occupied by each climate combination. Due to the highly skewed distribution of areas occupied (from 1 to 24000 km<sup>2</sup> for current climate), areas were log-transformed before applying the color scheme.

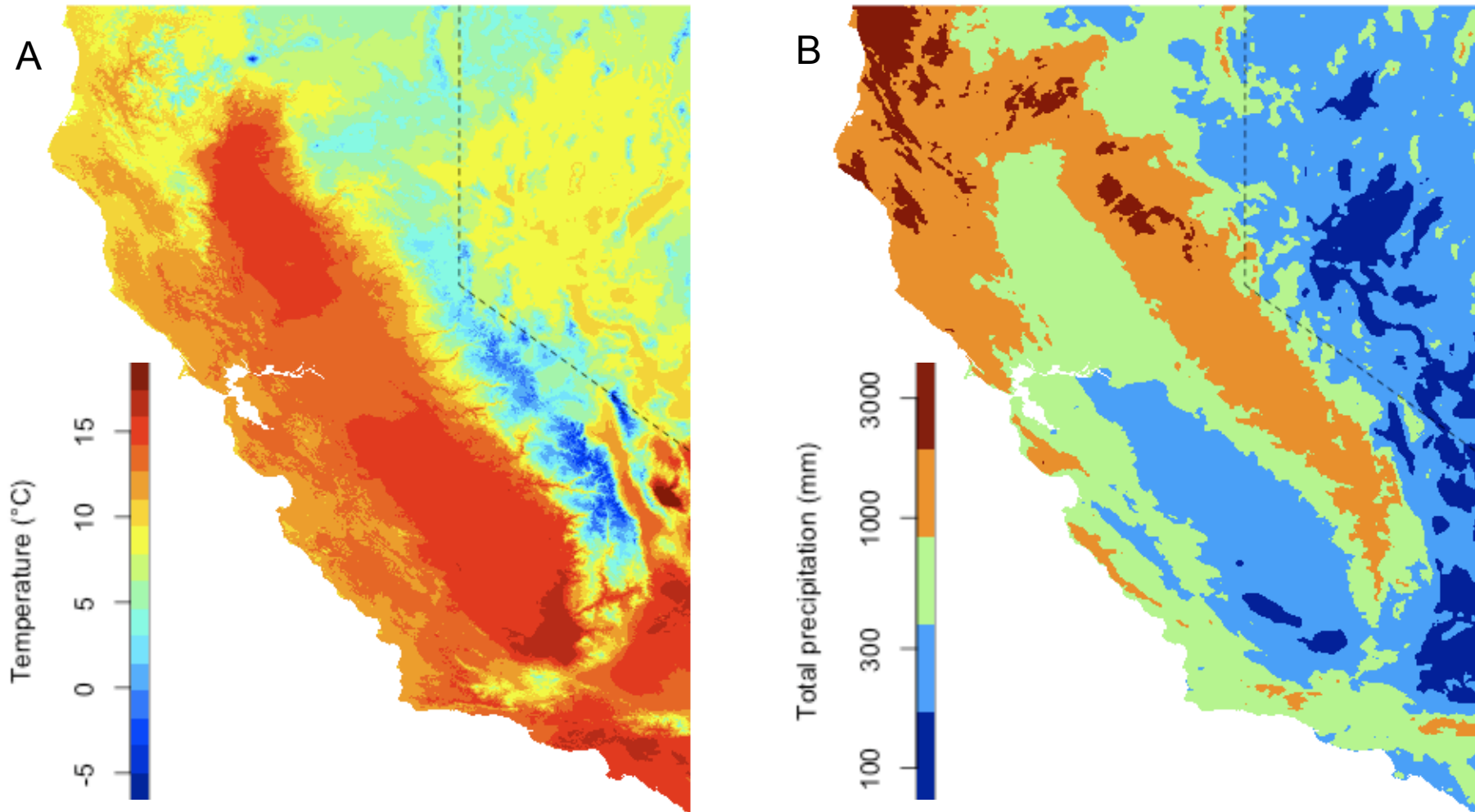


Fig. S7. Maps of mean annual temperature and total annual precipitation (log10 transformed) for the 1971-2000 historical period (PRISM). Color breaks correspond to histogram bins in Fig. S6, illustrating geographic distribution of climates that are classified in the same bin for each variable.

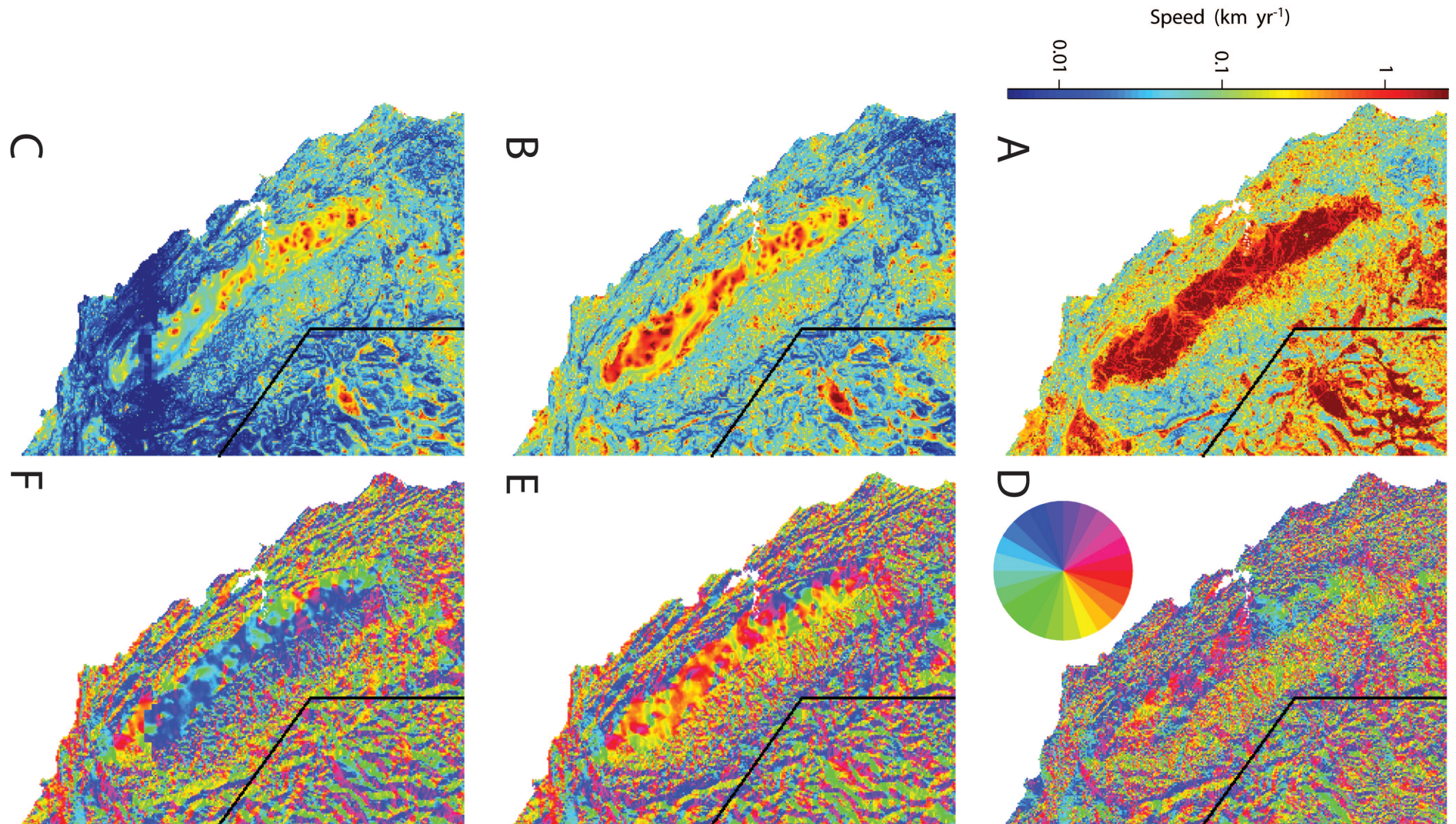


Fig. S8. Velocity (left) and direction (right) of climate change for temperature (A, D) and precipitation under the warmer-drier (B, E) and warmer-wetter (C, F) scenarios. Directions represent the direction of movement in space to offset projected changes in climate, and are shown using the compass wheel.